

Aqueous asymmetric pseudocapacitor featuring high areal energy and power using conjugated polyelectrolytes and ${\rm Ti_3C_2T_x}$ MXene

Yip, Benjamin Rui Peng; Chen, Chaofan; Jiang, Yan; Ohayon, David; Bazan, Guillermo C.; Wang, Xuehang

DOI

10.1038/s41467-025-63034-9

Publication date

Document Version Final published version Published in

Nature Communications

Citation (APA)
Yip, B. R. P., Chen, C., Jiang, Y., Ohayon, D., Bazan, G. C., & Wang, X. (2025). Aqueous asymmetric pseudocapacitor featuring high areal energy and power using conjugated polyelectrolytes and Ti C T MXene. *Nature Communications*, *16*(1), Article 7984. https://doi.org/10.1038/s41467-025-63034-9 2 x

Important note

To cite this publication, please use the final published version (if applicable). Please check the document version above.

Copyright

Other than for strictly personal use, it is not permitted to download, forward or distribute the text or part of it, without the consent of the author(s) and/or copyright holder(s), unless the work is under an open content license such as Creative Commons.

Please contact us and provide details if you believe this document breaches copyrights. We will remove access to the work immediately and investigate your claim.

nature communications



Article

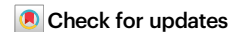
https://doi.org/10.1038/s41467-025-63034-9

Aqueous asymmetric pseudocapacitor featuring high areal energy and power using conjugated polyelectrolytes and $Ti_3C_2T_x$ MXene

Received: 2 November 2024

Accepted: 4 August 2025

Published online: 27 August 2025



Despite the development of various pseudocapacitive materials, full-cell pseudocapacitors have yet to surpass the power density of conventional electric double layer capacitors, primarily due to the lack of high-rate positive pseudocapacitive materials. This work reports a solid-state conjugated polyelectrolyte that achieves high-rate charge storage as a positive electrode, facilitated by a co-ion desorption mechanism. The conjugated polyelectrolyte retains 70% of its capacitance at 100 A g⁻¹ with a mass loading of 2.8 mg cm⁻² and exhibits a long cycling life of 100,000 cycles in a Swagelok cell configuration. Increasing the electrode thickness fourfold has minimal impact on ion diffusivity and accessibility, yielding a high areal capacitance of 915 mF cm⁻². When paired with a high-rate negative pseudocapacitive electrode Ti₃C₂T_x, the device leverages the redox-active potentials of both materials, achieving a device voltage of 1.5 V and supports operation rates up to 10 V s⁻¹ or 50 A g⁻¹. This configuration enables the pseudocapacitor to deliver an areal power of 160 mW cm⁻², while significantly increasing the areal energy (up to 71 μWh cm⁻²). The high areal performance, combined with the additive-free and water-based fabrication process, makes pseudocapacitors promising for on-chip and wearable energy storage applications.

Supercapacitors are energy storage devices that bridge the gap between conventional electrolytic capacitors and batteries¹. Electric double-layer capacitors (EDLCs) are the most widely used type of supercapacitor, complementing conventional batteries in applications that demand high power density². EDLCs utilize a surface-controlled process that stores charges by electrostatic adsorption of electrolyte ions on high surface area electrodes (i.e., activated carbon), thereby enabling high power density and extended cycle life. Organic

electrolytes are widely used in EDLCs, as they offer a wide voltage window and allow for good wettability of activated carbon, whose surface is often hydrophobic. In contrast, aqueous electrolytes are gaining attention due to their high rate performance and enhanced device safety, making them particularly appealing for applications where fire prevention and environmental safety are major concerns. However, the main limitation of aqueous electrolyte-based EDLCs is the narrow voltage window dictated by the thermodynamic potential

¹Departments of Chemistry and Chemical & Biomolecular Engineering, National University of Singapore, Singapo

of water (-1.2 V), which ultimately restricts the energy density³. One strategy to overcome this limitation is to replace one carbon electrode with another type of electrode material to make asymmetric supercapacitors⁴, enabling a device voltage of up to 2.0 V in aqueous electrolytes⁵. Using two different electrode materials would take advantage of two distinct electroactive windows, enabling the device to cover a wider voltage range before hydrolysis of water occurs. Despite improvements, the energy density is still limited by the low capacitance of carbon-based materials, which is typically addressed by enhancing the active surface area and optimizing the pore size distribution⁶. However, it has been noted that the capacitance of EDLCs remains constrained due to the limitation in achieving the maximum specific surface area of activated carbon, typically ranging between 3000 and 4000 m² g⁻¹⁶.

Pseudocapacitors are a subclass of electrochemical capacitors that store energy through fast and reversible redox reactions occurring at or near the surface of electrode materials. This process, known as the pseudocapacitive mechanism, involves surface redox reactions and/or pseudocapacitive intercalations⁷. Pseudocapacitive materials thus generally exhibit higher capacitance than carbon-based materials due to the added charge storage from redox processes8. Different types of materials have been reported to exhibit pseudocapacitance properties, including metal oxides, conjugated polymers, and twodimensional (2D) materials9. Among these materials, 2D MXenes, which comprise a family of transition metal carbides, nitrides, and carbonitrides, stand out for their high-rate pseudocapacitive charge storage capability^{10,11}. They offer a unique combination of high conductivity, hydrophilic surface, and flexible interlayer spacing, allowing highly reversible surface-mediated redox reactions to occur at high operating rates^{12,13}. $Ti_3C_2T_x$ in particular has shown volumetric capacitances of up to 1500 F cm⁻³ or a gravimetric capacitance of 380 F g⁻¹ in acidic electrolytes¹⁴. More importantly, $Ti_3C_2T_x$ with a macroporous architecture is able to deliver high-rate performance with >80% capacitance retention at a scan rate of 10 V s-114. However, the implementation of $Ti_3C_2T_x$ is constrained by its susceptibility to oxidation when operated above its open circuit potential (OCP), rendering it viable solely as a negative electrode, especially in aqueous electrolytes. Symmetric supercapacitors utilizing $Ti_3C_2T_x$ thus exhibit a restricted operating device voltage of approximately 0.6 V, which limits the maximum achievable energy density^{15,16}.

To expand the voltage window of Ti₃C₂T_x-based pseudocapacitors, asymmetric cells have been explored by pairing with other electrode materials. For instance, asymmetric devices have been fabricated using activated carbon as the positive electrode, resulting in wider cell voltages; however, this configuration is limited by the capacitance of activated carbon¹⁷. Ti₃C₂T_x devices with RuO₂ or Nb₂O₅ metal oxides have also been disclosed. Nevertheless, the cost of such noble metals may prevent widespread applications^{3,18}. Other metal oxides such as MnO₂ and MoO₃ have also been used, yet their rate capability is hindered due to their low intrinsic electrical conductivity^{19,20}. Alternatively, conjugated polymers have been modified with carbon-based materials to leverage the redox-active properties of the electronically delocalized backbone and the high conductivity of carbon; however, their rate capabilities remain behind that of $Ti_3C_2T_x^{21,22}$. Altogether, there exists opportunities to design and explore positive pseudocapacitive electrode materials that simultaneously offer high rate capability and cycling stability comparable to that of $Ti_3C_2T_x$.

Conjugated polyelectrolytes (CPEs) are a subset of conjugated polymers characterized by a conjugated backbone bearing ionic pendant groups²³. They are also classified as mixed electronic ionic conductors (OMIECs), offering ion conduction within the bulk material due to the presence of an ionic lattice inherent to their chemical structure²⁴. Since ion diffusion can be a key rate-limiting factor in energy storage devices, CPEs have emerged as a material of interest in

the development of novel electrochemical capacitors²⁵⁻²⁷. Our group has worked previously with CPE-K, a narrow bandgap CPE with anionic side chains (Fig. 1a). Solid-state CPE-K-based electrodes inherit the advantages of typical of CPEs, including water processability, potential for recyclability, and sufficient electrochemical stability²⁸. Moreover, due to its high electrical and ionic conductivity, CPE-K can deliver useful rate performances without the need for additives. For example, thin films of CPE-K (0.28 mg cm⁻²) are able to retain 85% of their original capacitance after 100,000 cycles at 25 A g⁻¹²⁹. Additionally, CPE-K can be reversibly electrochemically doped above its OCP making it an ideal candidate for high-rate positive electrodes, particularly when paired with MXene-based negative electrodes in aqueous supercapacitors.

While some existing pseudocapacitors exhibit high energy density, they often suffer from poor power performance, falling far short of EDLCs9. Conversely, EDLCs, typically those employing carbon electrodes, provide high power density but lack sufficient energy density. This creates a gap in energy storage technology, as no current device effectively combines both high energy and high power. We disclose herein, a Ti₃C₂T_x | | CPE-K pseudocapacitor that makes inroads toward solving this trade-off, offering a promising solution to bridge the divide between batteries and capacitors, a critical advancement for electrochemical energy storage. Central to this achievement is CPE-K, which enables a fast energy storage process through an uncommon "co-ion desorption" mechanism. As shown in Fig. 1a, unlike the typical counter-ion adsorption mechanism, co-ion desorption involves the expulsion of cations (co-ions) from the electrode upon charging. This mechanism minimizes steric effects during ion adsorption/intercalation, leading to high-rate performance at practical mass loadings exceeding 10 mg cm⁻² and cycling stability of up to 100,000 cycles. The fabrication of an asymmetric pseudocapacitor device using CPE-K as the positive electrode and Ti₃C₂T_r as the negative electrode enables operation up to 10 V s⁻¹ with a cell voltage of 1.5 V. It is possible to achieve an areal energy of up to 71 µWh cm⁻² and an areal power of up to 160 mW cm⁻² in a pouch cell configuration, and up to 38 uWh cm⁻² and 11 mW cm⁻² in a solid-state device. The straightforward fabrication process, water-based handling, and operation in aqueous electrolytes position Ti₃C₂T_x|| CPE-K pseudocapacitors as a relevant candidate for environmentally sustainable and cost-effective energy storage applications.

Results and discussion

Physical characterization of drop cast CPE-K films before and after doping

CPE-K was synthesized using polymerization protocols previously reported^{25,29}. The resulting crude CPE-K was precipitated in acetone, purified by dialysis (MWCO = 3500 kDa), and lyophilized to obtain a dark blue powder that is soluble in H₂O but insoluble in common polar organic solvents³⁰. It has previously been reported that CPE-K, which has a p-type backbone allows it to participate in redox reactions at positive potentials, making it promising for use as a positive electrode. In addition, CPE-K exhibits high rate capability; however, its charge storage mechanism remains uninvestigated. We postulate that upon doping of the CPE-K backbone, the pendant sulfonate groups stabilize the positive charge on the backbone, while the cation (K⁺ initially) undergoes desorption to obtain CPE⁺. When dedoped, cations would be re-adsorbed into bulk CPE material. The readsorbed cation depends on the electrolyte composition and in this work, H⁺ from the H₂SO₄ electrolyte is expected to be adsorbed. After the first cycle, the material would thus be more accurately referred to as CPE-H. This mechanism may be beneficial for high-rate charge storage as a positive electrode in energy storage devices (Fig. 1a). This is because the charging process of co-ion desorption facilitates ion diffusion by minimizing steric effects³¹. To confirm this hypothesis, several characterizations were carried out.

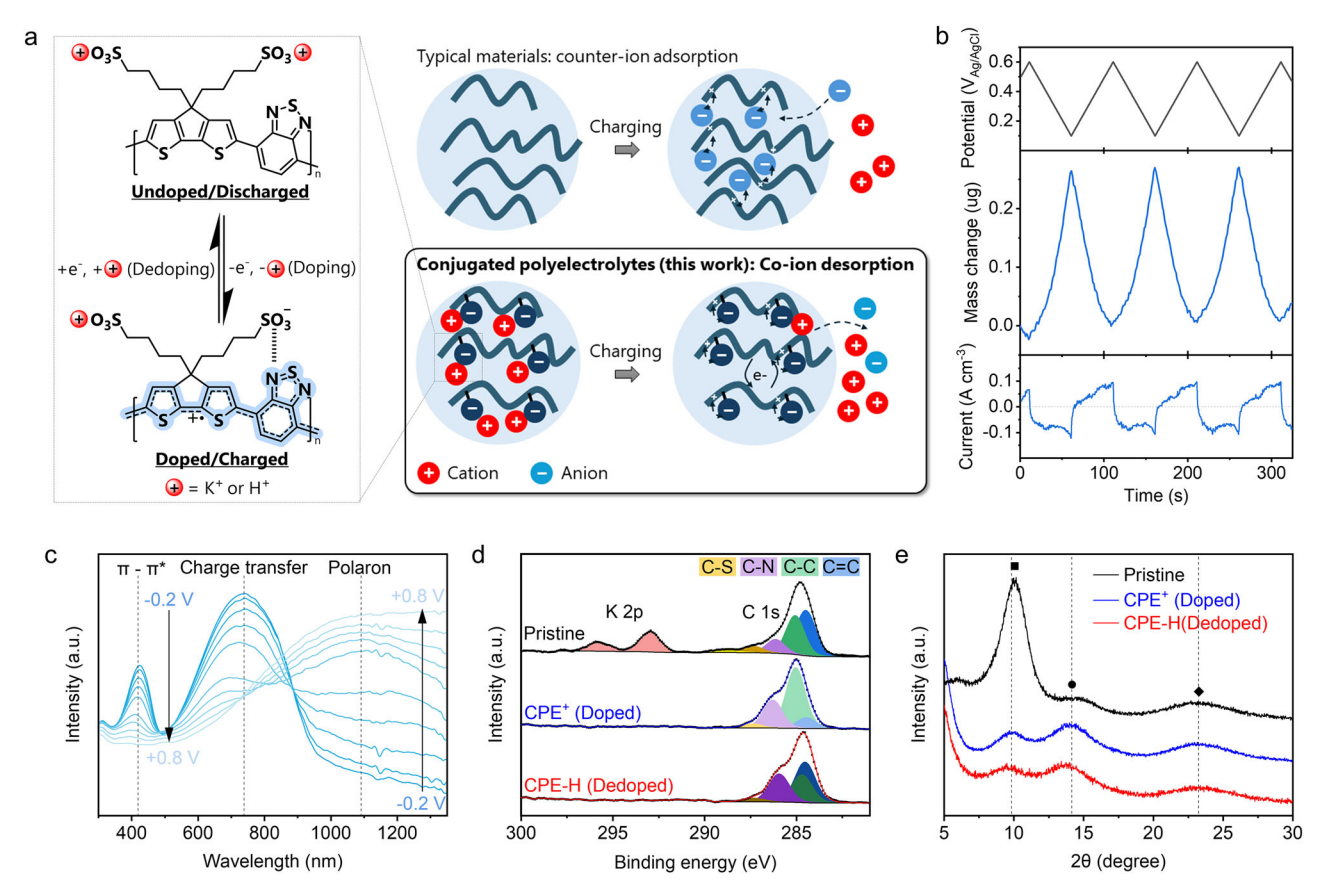


Fig. 1 | **Structure and characterizations of CPE-K film at its pristine, doped and undoped states. a** Chemical structures of CPE-K upon electrochemical doping/charging and dedoping/discharging and the difference in ion uptake in CPEs compared to typical energy storage materials. **b** Mass change during potentiometric charging of spin cast CPE-K using in situ Electrochemical Quartz Crystal

Microbalance. **c** Spectroelectrochemistry of CPE-K at different potentials. **d** High-resolution XPS spectra of the K 2p and C 1s regions of CPE-K in its pristine, doped, and dedoped states. **e** XRD patterns of CPE-K in its pristine, doped, and dedoped states. **e** And \bullet represent lamellar peaks while \bullet represent π - π stacking peaks.

First, we performed spectroelectrochemical analysis of a CPE-K film in 1.0 M H₂SO₄, to confirm the occurrence of reversible doping and dedoping in acidic electrolyte. CPE-K was spin-cast on an ITOcoated glass slide and used as the working electrode. A quartz cuvette was used as the cell, while a silver wire acted as a pseudo-reference electrode and a platinum wire as the counter electrode. We recorded the spectrum at the open circuit voltage (OCV), which is approximately 0.3 V vs Ag/AgCl, denoted as the black trace in Fig. 1c. The absorbance of CPE-K at different potentials is shown in Fig. 1c. We identified three characteristic transitions: 400 nm, corresponding to the π - π transition; 700 nm, corresponding to intramolecular charge transfer; and 1180 nm, corresponding to polaron absorption. CPE-K as obtained post purification is doped, as evidenced by the presence of the polaronic peak at its open circuit voltage. By sweeping the voltage from -0.2 to 0.8 V, one observes that the π - π and charge transfer bands decrease, while the polaron contribution increases. Spectroelectrochemistry results are thus consistent with oxidation of the conjugated backbone of CPE-K and highlights the presence of electrochemical doping in the charge storage mechanism.

To obtain more insight into the morphological changes of CPE-K upon electrochemical doping, SEM imaging was carried out on the surface and cross sections of CPE-K at different electrochemical states (Fig. S4). Briefly, CPE-K was drop cast atop gold-coated substrates at a mass loading of approximately 1.0 mg cm $^{-2}$. The first state, termed here as pristine, was CPE-K Film analyzed after drop cast. To obtain CPE $^{+}$ and CPE-H states, CPE-K films were subjected to a bias of $\pm 0.8 \, \text{V}$ and then $\pm 0.2 \, \text{V}$ vs Ag/AgCl using 1.0 M H₂SO₄ as the electrolyte, corresponding to the potentials required for achieving doped and

dedoped states, respectively. Cross-sectional and surface SEM revealed a homogeneous and generally amorphous macrostructure in the pristine state (Fig. S4a). The surface SEM image of the pristine film shows a ridge-like morphology reminiscent of a dewetting pattern (Fig. S4d). These patterns create nanometer-wide channels, which are known to enhance electrolyte uptake and ionic transport by providing a porous structure accessible to the electrolyte and shortening ion diffusion lengths from the bulk electrolyte to the electrode surface^{32,33}. The formation of this desirable morphology may be attributed to the increase in surface tension during drop casting as the droplet becomes more concentrated while drying. The surface SEM after electrochemical charging (Fig. S4e) exhibits more defined grain boundaries when compared to the pristine state (Fig. S4d), suggesting restructuring into a more ordered state. After discharging, surface SEM analysis reveals an increase in grain size compared to the charged/doped state CPE⁺ (Fig. S4f). We reason that CPE-K undergoes a mechanism in which K+/H+ ions desorb upon electrochemical doping and adsorb upon electrochemical dedoping. Overall, SEM results suggest behavior consistent with co-ion uptake upon electrochemical charging, as evidenced by the smaller grain sizes in the charged/doped state CPE+ when compared to the uncharged/dedoped state.

Qualitative ex-situ X-ray photoelectron spectroscopy (XPS) analysis was performed to probe the presence of K⁺ ions while at the same time monitoring the changes in the conjugated backbone upon electrochemical cycling. CPE-K at different electrochemical states were analyzed following the same electrochemical doping procedure above. Figure 1c shows the high-resolution XPS spectra of the C 1s and K 2p regions of Pristine (CPE-K), Doped (CPE⁺), and Dedoped (CPE-H)

samples. As anticipated, the Pristine sample consists of three distinct peaks, namely the C 1s peak at 284.6 eV, the K $2p_{3/2}$ peak at 292.8 eV, and the K $2p_{1/2}$ peak at 295.6 eV, in agreement with previous reports³². Upon electrochemical doping, one observes a disappearance of the K⁺ signals, suggesting that the majority of K⁺ ions are expelled upon oxidation of the backbone. Dedoping of CPE⁺ (-0.2 V) does not return the K⁺ ions. This is most reasonably due to large excess of H⁺ from the H₂SO₄ electrolyte, replacing K⁺ as the main charge compensating cation within the original CPE-K film, thus becoming CPE-H. Overall, exsitu XPS supports the hypothesis of the co-ion desorption mechanism, as it reveals the elimination of K⁺ ions upon electrochemical charging.

The XPS C 1s contribution could also be deconvoluted into 4 distinct peaks. The peak at 284.5 eV is assigned to the conjugated backbone (C = C), the peak at 285.1 eV is associated with carbons in the alkyl chain (C-C), the peak at 286.1 eV corresponds to C-S, and the peak at 287.3 eV corresponds to carbons bonded to nitrogen atoms (C=N). The additional peak at 289.0 eV is attributed to a π - π shake-up satellite peak³². The peak intensity ratios for Pristine CPE-K is 0.16 (C=N): 0.35 (C-S): 1.00 (C-C): 1.24 (C=C). Based on the assumption that the alkyl carbons remain unaffected by doping, there is a significant decrease in the C=C and C=N components upon doping, exhibiting peak intensity ratios of 0.06:0.46:1.00:0.18. This change is consistent with the fact that, in the oxidized state, there is depletion of electron density in the π bonds, which gives rise to less intense C=C and C=N components. Conversely, Dedoped CPE-K exhibits peak intensity ratios of 0.13:1.00:1.00:1.46, consistent with the fact that the C=N and C=C bonds are restored after reduction of the backbone. Overall, XPS fitting results shows changes consistent with oxidation and a return to the ground state of the CPE-K backbone.

X-ray diffraction was carried out to probe the changes in packing upon electrochemical doping of CPE-K. The results of these studies are summarized in Fig. 1d. Pristine CPE-K films predominantly exhibit a peak at $2\theta = 10.1^{\circ}$, a less intense peak at $2\theta = 14.7^{\circ}$, and a broad peak at $2\theta = 23.3^{\circ}$, suggesting that slow evaporation from water promotes the formation of crystalline domains (Fig. 1d). The diffraction peak at $2\theta = 10.1^{\circ}$ corresponds to a Bragg spacing of d = 8.8 Å in agreement with previously reported data²⁹. This also aligns with previously reported GIWAXS measurements on spin coated CPE-K films, which also exhibited similar scattering features $(q_z = 0.75 \,\text{Å}^{-1}, \, d = 8.3 \,\text{Å})^{33}$. As in previous reports, the peak at $2\theta = 10.1^{\circ}$ may also be viewed as an ionic lattice that would facilitate ion mobility³³. The more diffuse peak at $2\theta = 23.3^{\circ}$, which corresponds to a d-spacing of 3.8 Å, is most reasonably assigned to π - π spacing. When electrochemically doped (CPE⁺), changes are observed in the lamellar region. For CPE⁺, the lamellar peak at $2\theta = 10.1^{\circ}$ decreased in intensity, while the higher lamellar peak $2\theta = 14.7^{\circ}$ increased in relative intensity, suggesting lamellar rearrangement. In addition, the lamellar peaks shifted to $2\theta = 9.8^{\circ}$ and 14.0°, corresponding to d-spacings of 9.0 Å and 6.3 Å, respectively, with the π - π peak (2θ = 23.3°) remaining unchanged. Dedoping of the polymer to from CPE+ to CPE-H did not reveal any changes in peak relative intensity in XRD patterns compared to CPE⁺. It is worth noting, however, the lamellar peaks when dedoped (CPE-H) are $2\theta = 9.6^{\circ}$ and 13.7° , which corresponds to a d-spacing of 9.2 Å and 6.5 Å, respectively. This corresponds to a 0.2 Å increase in lamellar spacing upon discharging, which we attribute to the increase in crystallite size upon uptake of H⁺ ions. Hence, XRD supports the co-ion desorption mechanism, consistent with our observations from SEM and XPS.

We investigated the mass change in CPE-K using in situ Electrochemical Quartz Crystal Microbalance (EQCM) on spin-cast CPE-K in 1.0 M H₂SO₄, which provides real-time insights into mass changes of the electrodes during electrochemical processes. A potential range of 0.1–0.6 V was used to eliminate side reactions from oxygen and water oxidation. The mass change of CPE-electrode was monitored for three cycles, indicating high reproducibility (Fig. 1b). As shown in Fig. 1b, the

positive sweeping of the potential, which corresponds to charging/doping, leads to a mass decrease in the CPE-based electrode material. Conversely, the negative sweeping of the potential, which corresponds to discharging/dedoping, result in an increase in the mass of the CPE bulk material. At the same time, the current response as a function of time is consistent with the doping and dedoping of CPE, confirming that oxidation is accompanied by mass decrease and vice versa. These experimental results, especially EQCM, support a charge storage mechanism of CPE-K that operates through a co-ion desorption process (Fig. 1a). When charged, the negatively charged sulfonate groups on the pendants compensate for the evolving positive charges on the backbone while simultaneously expelling the cations. When discharged, cations migrate back into CPE-K to maintain charge neutrality.

Electrochemical characterization of drop cast CPE-K films

The rate performance of CPE-K film electrodes has been previously examined up to a loading density of 2.3 mg cm⁻², which precludes practical applications²⁹. Accordingly, we sought to characterize CPE-K electrodes at larger loading densities, specifically 2.8, 5.6, 8.4, and 11.2 mg cm⁻²³⁴. CPE-K film electrodes were prepared by a simple drop cast process from water²⁹. We evaluated the performance of CPE-K as a positive electrode material using a three-electrode Swagelok cell setup. We chose 1.0 M H₂SO₄ as the electrolyte as it not only gives the best rate performance for CPE-K with an extended potential window of up to 0.8 V vs Ag/AgCl, but also because Ti₃C₂T_x exhibits highest specific capacitance with H₂SO₄ as well. Though a slightly better rate performance was observed in higher-concentration H₂SO₄ electrolyte (Fig. S7a), we used 1M H₂SO₄ due to its lower corrosiveness. A potential window of +0.8 V to -0.2 V vs Ag/AgCl was chosen based on a Coulombic efficiency of >99% (Fig. S7b) to ensure reversible charge and discharge of the CPE-K electrode in H₂SO₄ electrolyte. As seen in Fig. 2a, the CPE-K film electrode exhibits pseudocapacitive characteristics in the cyclic voltammetry traces at all loading densities (Fig. S7)^{26,29}. CV was conducted at high scan rates (>1000 mV s⁻¹) to evaluate the performance under rapid charging/discharging, an essential requirement for high-power applications. Moreover, these measurements provide insight into CPE-K's capacitive behavior, charge storage capability, ion transport efficiency, and electrochemical stability under high-power conditions. We analyzed the peak current and scan rate relationship using Eq. (1):

$$i = av^b \tag{1}$$

where i is the peak current, a is an arbitrary constant, v is the scan rate and b is a value between 0.5 to 1.0. The b-value can be obtained from the slope of the plot of $\log i$ versus $\log v$, where a b-value of ~ 1.0 indicates fast reversible surface-controlled kinetics, while a b value of ~ 0.5 indicates a diffusion-limited process. Figure 2b shows the relationship between the $\log i$ versus $\log v$, and we found a b-value of ~ 1.0 for all loading densities below $500 \, \mathrm{mV \, s^{-1}}$, indicativ of fast reversible surface-controlled kinetics. At scan rates $> 1000 \, \mathrm{mV \, s^{-1}}$ CPE-K film electrodes become more diffusion-limited since the b-value starts to decrease below 1. In particular, the b-value dips to $0.87, 0.75, 0.50, \mathrm{and} \, 0.40$ in order of increasing loading density at $10 \, \mathrm{V \, s^{-1}}$. It is worth noting that the b value of the CPE-K film electrode at $11.2 \, \mathrm{mg \, cm^{-2}}$ drops to a value below $0.5, \mathrm{which}$ means that the electrode is too thick to be operated at $10 \, \mathrm{V \, s^{-1}}$.

Figure 2d shows the galvanostatic charge-discharge (GCD) trace of the 11.2 mg cm⁻² CPE-K film electrode at specific currents of 2.5 A g⁻¹ to 50 A g⁻¹. One observes a nearly triangular trace, indicating fast surface-controlled kinetics. A slight deviation from linearity is observed at potentials between 0.0 and 0.15 V vs Ag/AgCl, corresponding to the oxidation onset (Fig. 2a). The specific capacitance can

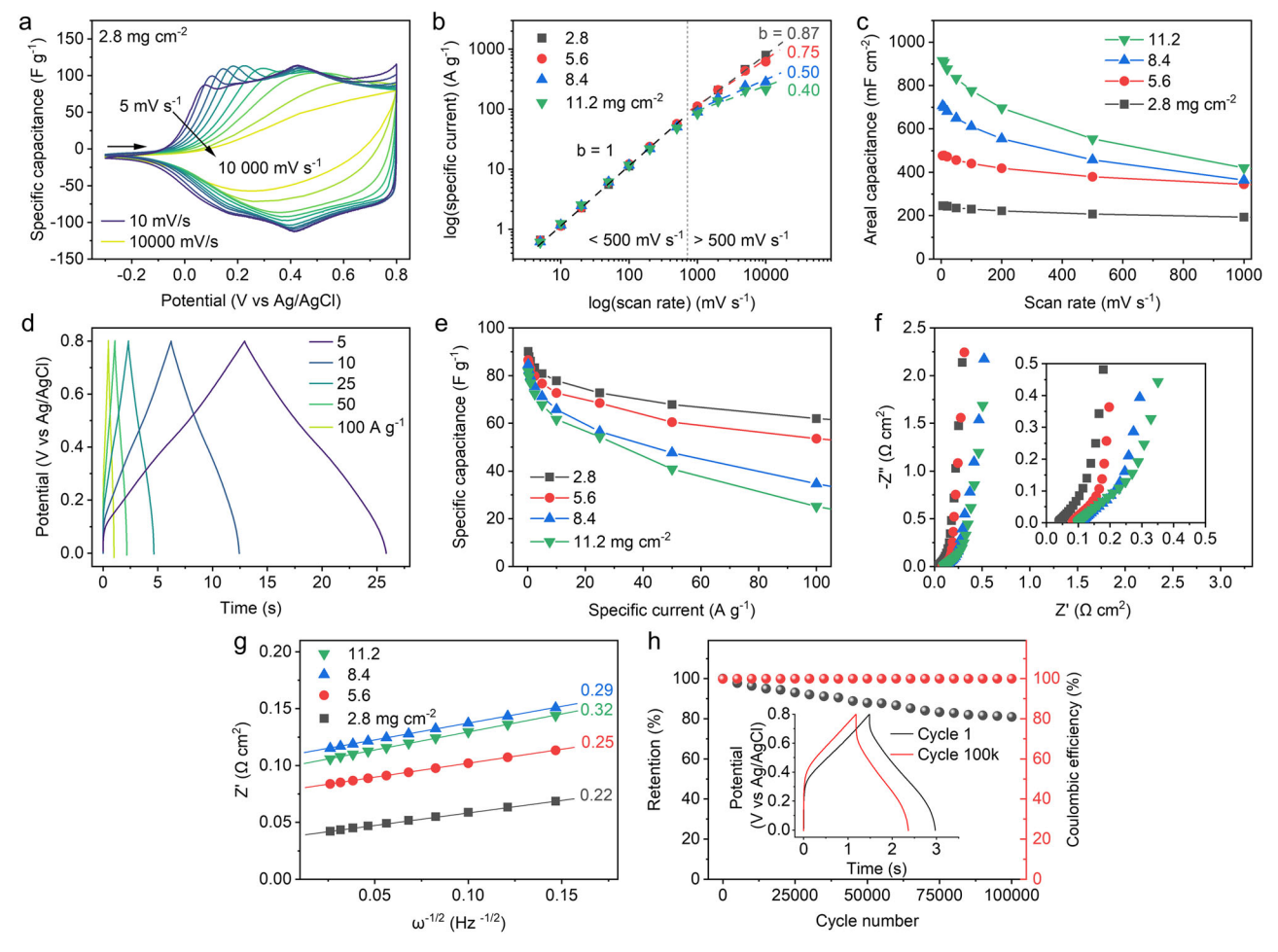


Fig. 2 | Electrochemical performance of drop-cast CPE-K on glassy carbon electrodes in 1.0 M $\rm H_2SO_4$ using a three-electrode configuration. a Representative cyclic voltammogram from 5 to 10 000 mV s⁻¹ of CPE-K electrode (11.2 mg cm⁻²). b Log-log plot of specific current versus scan rate showing decreasing b values at high scan rates and mass loadings. c Areal capacitance of CPE-K electrodes as a function of increasing scan rates. d Representative GCD

curves of CPE-K electrode (11.2 mg cm⁻²) from 2.5 to 50 A g⁻¹. **e** Specific capacitance of CPE-K electrodes at different mass loadings as a function of increasing specific current. **f** Nyquist plots of CPE-K at different mass loadings obtained from EIS. **g** Linear fit of Z' versus $\omega^{-1/2}$ to obtain the Warburg coefficient, σ . **h** Cycling stability of 11.2 mg cm⁻² CPE-K electrode cycled at a specific current of 25 A g⁻¹.

be calculated for a non-linear GCD using Eq. (2):

$$C_{\rm S} = I \int \frac{1}{V(t)} dt \tag{2}$$

where *I* is the applied specific current, *t* is the discharge time and V(t) is the discharge trace in potential as a function of *t*. CPE-K film electrodes deliver a specific capacitance of up to $90 \, \mathrm{F \, g^{-1}}$ (252 mF cm⁻²) at 2.8 mg cm⁻² at a specific current of $0.25 \, \mathrm{A \, g^{-1}}$. At a specific current of $50 \, \mathrm{A \, g^{-1}}$, CPE-K electrode of mass loading $2.8 \, \mathrm{mg \, cm^{-2}}$, exhibited a capacitance retention of 75% ($68 \, \mathrm{F \, g^{-1}}$, $190 \, \mathrm{mF \, cm^{-2}}$). It is also worth noting that the specific capacitance of CPE-K only decreases to $81 \, \mathrm{F \, g^{-1}}$ ($915 \, \mathrm{mF \, cm^{-2}}$) when the loading density is increased fourfold, up to $11.2 \, \mathrm{mg \, cm^{-2}}$. This suggests that CPE-K film electrodes display enhanced ionic transport properties, as most of the electrochemically active sites are still accessible despite a fourfold increase in thickness. In particular, an $11.2 \, \mathrm{mg \, cm^{-2}}$ CPE-K film electrode maintains $41 \, \mathrm{F \, g^{-1}}$ ($459 \, \mathrm{mF \, cm^{-2}}$) at a specific current of $50 \, \mathrm{A \, g^{-1}}$, which corresponds to a capacitance retention of 50%.

Electrochemical impedance spectroscopy (EIS) was carried out and the results are presented in the form of Nyquist plots normalized to the areal impedance (Fig. 2f). CPE-K film electrodes generally show low charge transfer resistance, as evidenced by the lack of a semi-circle

at all loading densities. Additionally, the ESR remains <0.1 Ω cm² and increases only slightly with increasing loading density increases, suggesting overall low internal resistance and facile ion accessibility. An obvious trend is the lengthening of the Warburg region as the loading density increases. This can be quantified using the Warburg diffusion coefficient, σ , which can be obtained from the slope of the relationship between Z' and the inverse square root of the frequency based on Eq. (3):

$$Z' = R_e + R_{ct} + \sigma \omega^{-\frac{1}{2}}$$
 (3)

where R_e is the equivalent series resistance, R_{ct} is the charge transfer resistance and ω is the frequency. From Fig. 2g, the Warburg diffusion coefficient correlated with the loading density, echoing the b-values obtained above. It is worth noting that the increase in the Warburg diffusion coefficient is minimal, increasing from 0.22 to 0.32 Ω s^{-1/2} despite a fourfold increase in loading density, suggesting facile ion diffusion within the CPE-K bulk material. The equivalent circuit model and fitting results are provided in the Supporting Information as Fig. S8 and Table S1. Finally, the cycling stability was evaluated using GCD cycles with an 11.2 mg cm⁻² CPE-K film to simulate practical mass loadings. The CPE-K electrodes retained 81% of their original capacitance after 100,000 cycles at 25 A g⁻¹, which may not represent

a groundbreaking advancement within the broader field of doublelayer capacitors. However, this performance exceeds typical values reported for pseudocapacitors by an order of magnitude, particularly those utilizing conjugated polymers. which is up to 2 orders of magnitude higher than other organic pseudocapacitive materials³⁵.

Recent studies have emphasized the importance of reporting areal capacitance alongside gravimetric and volumetric capacitances, as areal capacitance better reflects the practical capabilities of electrodes when integrated into energy storage devices especially microsupercapacitors, where areal capacitances are normally evaluated³⁴. The areal capacitance of CPE-K film electrodes versus scan rate is provided in Fig. 2c reveals an areal capacitance of up to 910 mF cm⁻² at 10 mV s⁻¹ with a loading of 11.2 mg cm⁻². When the scan rate was increased to 100 mV s⁻¹, the areal capacitance dropped to 780 mF cm⁻², which corresponds to 86% capacitance retention. For a broader perspective, Fig. 2i compares the areal capacitance and rate performance of the 11.2 mg cm⁻² CPE-K film electrode against other state-of-the-art pseudocapacitive materials, highlighting the competitive performance of CPE-K, especially at high-rates of operation.

The enhanced performance of CPE-K electrode is due to its high ion diffusivity and ion accessibility, even at increased thicknesses. Despite a fourfold increase in thickness, from 2.8 mg cm⁻² to 11.2 mg cm⁻², the Warburg coefficient shows only a minimal increase from 0.22 to $0.32 \Omega s^{-1/2}$ (Fig. 2g), indicating that the high ion diffusivity remains unimpaired. Meanwhile, areal capacitance rises from 245 to 910 mF cm⁻², indicating that 93% of CPE-K's charge-storing capability remains active despite the fourfold increase in the electrode thickness. This high utilization demonstrates great ion accessibility within the thick CPE electrodes. The kinetic behavior of the CPE electrode can be attributed to its unique structure. As shown in Fig. 1a, CPE-K stores charge through a polymeric redox process accompanied by cation desorption. This co-ion desorption mechanism facilitates faster kinetics due to the presence of less steric hindrance³¹. Additionally, the charge storage kinetics in CPE-K also benefit from the electronic-ionic coupling effect characteristic of OMIECs, which provides high ionic and electronic conductivity. Moreover, the observed π - π stacking in the drop-cast electrode is crucial not only for electronic charge transport but also for rapid ion diffusion³⁶. Therefore, CPE-K electrodes, free from additives and binders, exhibit intrinsically good electronic and ionic transport and can be directly employed to achieve enhanced high-rate performance and accommodate large mass loadings for high areal capacitance. Notably, the absence of additives and binders is expected to increase the mass fraction of active material in the device, further benefiting the overall energy and power density in full cells.

Synthesis and electrochemical characterization of drop cast $Ti_3C_2T_x$ films

Based on the pseudocapacitive profile of CPE-K films described above, we sought to fabricate devices with the known negative electrode $Ti_3C_2T_x^{-14}$. Prior to fabricating the full device, it is useful to obtain the three-electrode electrochemical performance of $Ti_3C_2T_x$ to carry out proper mass balancing. Ti₃C₂T_x MXene was synthesized using selective etching of Ti₃AlC₂ precursor using the in situ HF etching method as reported previously³⁷. As shown in Fig. S3, the XRD pattern of MXene shows characteristic (001) peaks, indicating an ordered layered structure. Compared to the XRD pattern of the MAX phase, the disappearance of the (104) peak and the shift of the (002) peak to lower angles indicate the removal of the A-layer, confirming the successful synthesis of MXene³⁸. The resulting $Ti_3C_2T_x$ colloidal solution can be processed into electrodes by various methods, including spray coating and/or spin coating on a variety of substrates, or can be membrane filtered into free-standing film electrodes. For the purpose of characterization, Ti₃C₂T_x was drop-cast on silicon substrates for XRD and SEM imaging. Drop-cast $Ti_3C_2T_x$ film exhibited a set of (00 l) peaks in the XRD spectrum, suggesting that it self-assembled into an aligned configuration (Fig. S3). The (002) peak with a 2θ = 5.8° corresponds to a d-spacing of approximately 1.5 nm, which is close to reported $Ti_3C_2T_x$ films with ordered stacking³⁹. This is further supported by cross-sectional SEM images which show a characteristic layered structure (Fig. S5). In addition, cross-sectional SEM revealed that the thickness of $Ti_3C_2T_x$ films ranged from approximately 3 to 13 µm for mass loadings of 0.85 to 3.4 mg cm⁻² (Fig. S5). Similar to the fabrication of CPE-K film electrodes, $Ti_3C_2T_x$ colloidal solution (10 µL, 3 mg mL⁻¹) was drop-cast on glassy carbon electrodes with a diameter of 3 mm and allowed to dry at ambient conditions.

We evaluated the performance of $Ti_3C_2T_x$ as a negative electrode material by using a three-electrode Swagelok cell setup. Drop-cast Ti₃C₂T_r electrodes exhibited a CV trace typical of Ti₃C₂T_r in H₂SO₄ electrolyte (Fig. S9a)14,40. This is attributed to the surface redox mechanism, where the change in the oxidation state of Ti and the transformation between -OH and =O surface groups are accompanied by (de-)intercalation of H $^+$ (from) into the interlayer of Ti₃C₂T_x 37 . $Ti_3C_2T_r$ shows a specific capacitance of 235 F g⁻¹ (226 – 396 mF cm⁻²) at low specific currents (<0.5 A g⁻¹, see Fig. S9d). At the mass loadings tested (0.96 to 1.9 mg cm⁻²), Ti₃C₂T_x film electrodes show signs of diffusion limitations due to the restacking of MXene layers. In particular, a log-log analysis shows b-values < 1 at all scan rates. Unlike CPE-K, the b-value of Ti₃C₂T_x starts to deviate from 1 even at low scan rates (5–100 mV s⁻¹). Nevertheless, a 1.9 mg cm⁻² Ti₃C₂T_x electrode can still achieve 250 mF cm⁻², or 63 % of its original capacitance (396 mF cm⁻²), at 1000 mV s⁻¹, which has a comparable performance with a 5.6 mg cm⁻² CPE-K electrode, despite the slightly lower areal capacitance (Fig. S9h). Notably, no obvious IR drop was observed from GCD at specific currents of 50 A g⁻¹ (Fig. S9c), suggesting low internal resistance. Cycling stability studies, determined by using repeated GCD cycles at 25 A g⁻¹, revealed 87% capacitance retention after 100,000 cycles. EIS measurements show that the ESR does not change significantly as the mass loading increases (Fig. S9f). In fact, the extent of ionic diffusion does not increase much, where the Warburg coefficient increased from 2.5 to 3.0 Ω s^{-1/2} despite a twofold increase in mass loading (Fig. S9e). Collectively, the three-electrode measurements show that drop-cast CPE-K and Ti₃C₂T_x electrodes are complementary pseudocapacitive platforms as they exhibited comparable rate performances (Fig. S9h).

Electrochemical characterization of $Ti_3C_2T_x \mid \mid$ CPE-K asymmetric pseudocapacitor in a Swagelok cell configuration

Asymmetric pseudocapacitors were fabricated using $Ti_3C_2T_x$ as the negative electrode and CPE-K as the positive electrode. We examined different Ti₃C₂T_x and CPE-K ratios to identify the best performance. Briefly, asymmetric pseudocapacitors of Ti₃C₂T_x and CPE-K were fabricated using Swagelok cells at mass ratios of 1:2.5, 1:3.0, 1:3.5 and 1:4.0 Ti₃C₂T_x:CPE-K (Fig. S10). The maximum cell voltage was determined through consecutive CVs with 100 mV increment starting from a cell voltage of 0.6 V. The appearance of a "tailing peak", signifying the presence of irreversible electrode reactions such as material breakdown or gas evolution reactions (Fig. 3a). We identified the maximum voltage window to be the voltage range within which the Coulombic efficiency is above 96% (Table S2). The mass ratio of 1:3 Ti₃C₂T_x:CPE-K gave the broadest voltage window of 1.5 V, with the highest capacitance: 32 F g⁻¹ (Fig. 3a). Increasing the amount of Ti₃C₂T_x with respect to CPE-K generally gave higher capacitance of the cell. However, too high Ti₃C₂T_x:CPE-K ratios may not be optimal as it may cause CPE-K to polarize beyond its electroactive window, leading to an earlier onset of irreversible reactions (e.g. polymer oxidation, gas evolution) and in turn, a smaller voltage window (Fig. S10a). This is evident when testing the cell with a Ti₃C₂T_x:CPE-K mass ratio of 1:2.5, where the maximum potential window was only 1.3 V. Therefore, the 1:3.0 Ti₃C₂T_x mass ratio offers an optimal balance between maximizing voltage window and

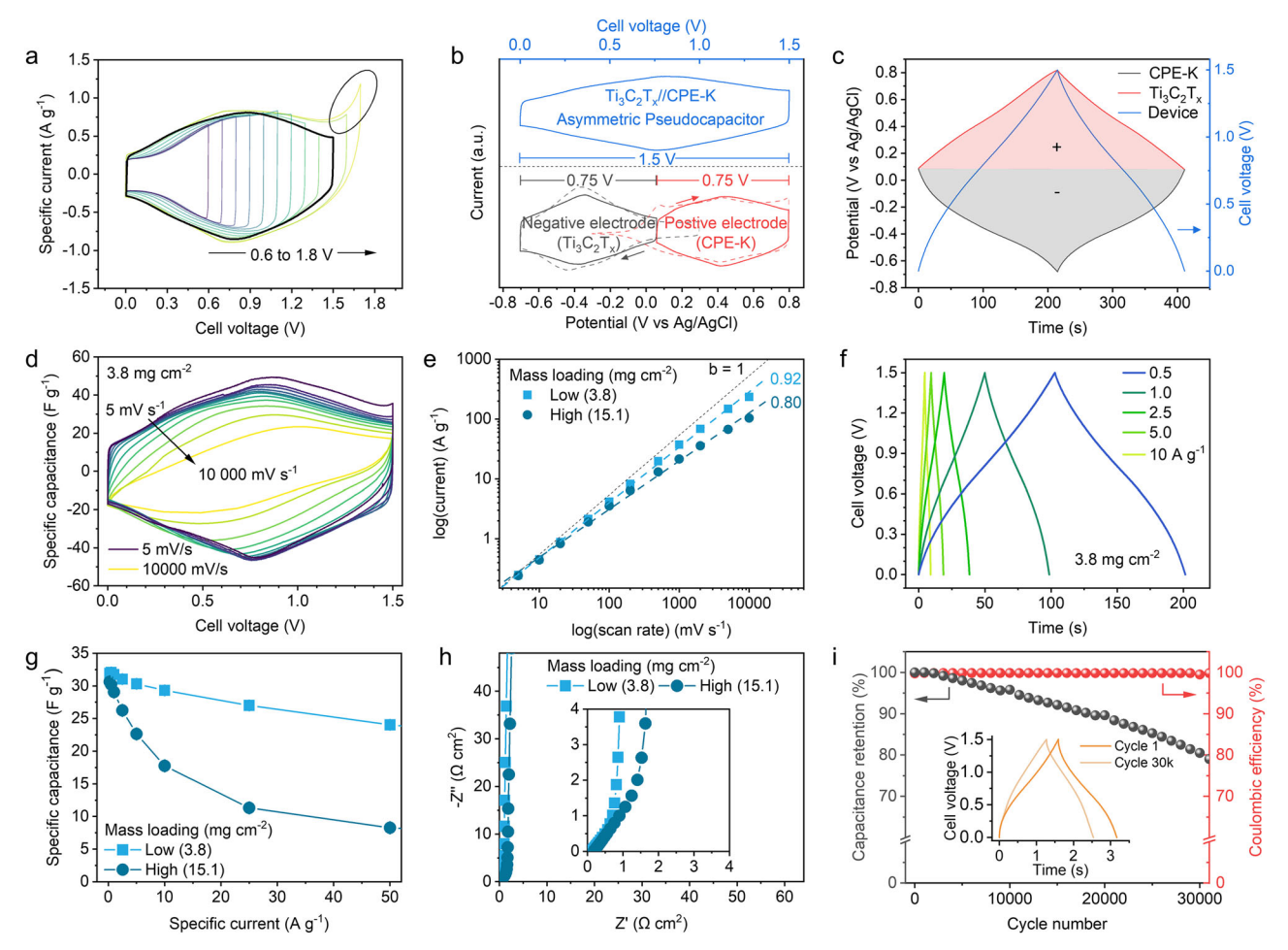


Fig. 3 | **Electrochemical performance of Ti**₃**C**₂**T**_x | |**CPE-K Swagelok cells in 1.0 M H**₂**SO**₄. **a** Optimization of device potential window by increasing the cell voltage. **b** Cyclic voltammogram of the full device and butterfly plot of the individual electrode potentials when charged in the device. **c** GCD trace of the individual electrode potentials and the full device. **d** Cyclic voltammograms Ti₃C₂T_x||CPE-K device at 3.8 mg cm⁻² from 5 to 10 000 mV s⁻¹. **e** Log-log plot of current versus scan

rate of low and high mass loading Ti $_3$ C $_2$ T $_x$ || CPE-K device. **f** GCD trace of Ti $_3$ C $_2$ T $_x$ || CPE-K device at 2.5–10 A g $^{-1}$ (3.8 mg cm $^{-2}$). **g** Specific capacitance of Ti $_3$ C $_2$ T $_x$ ||CPE-K device as a function of increasing specific current. **h** Nyquist plot of Ti $_3$ C $_2$ T $_x$ ||CPE-K device. **i** Cycling stability of 3.8 mg cm $^{-2}$ Ti $_3$ C $_2$ T $_x$ ||CPE-K device at a specific current of 25 A g $^{-1}$.

capacitance, while minimizing the risk of irreversible electrode side reactions.

We recorded the CV and GCD curves of each electrode when cycling the full cell between 0.0 and 1.5 V (the maximum voltage of 1:3 Ti₃C₂T_x:CPE-K cell) with the intent of understanding the charging behavior of each electrode. Figure 3b shows CV traces of individual positive and negative electrodes in the form of a "butterfly plot" overlayed with the voltammogram of the Ti₃C₂T_r | | CPE-K device⁴¹. The butterfly plot illustrates that both electrodes experienced an equal extent of polarization of 0.75 V. When the device is at 0.0 V, the open circuit voltages of Ti₃C₂T_x and CPE-K are at approximately 0.05 V vs Ag/AgCl. When the device is charged to 1.5 V, $Ti_3C_2T_x$ polarizes to -0.7 V vs Ag/AgCl, whereas CPE-K polarizes to +0.8 V vs Ag/AgCl, which are aligned with their pseudocapacitive windows (Fig. 3b). In addition, GCD also allows us to track the individual electrode potentials upon charging, highlighting the complementary potential windows in the "diamond plot" shown in Fig. 3c. Together, the complementary potential windows of both electrodes enable the operation of the device in aqueous media with an extended potential range at an optimal mass ratio.

We further evaluated the 1:3 $\text{Ti}_3\text{C}_2\text{T}_x$ || CPE-K devices with total mass loadings of 3.8 and 15.1 mg cm⁻². The CV profile of the $\text{Ti}_3\text{C}_2\text{T}_x$ || CPE-K device exhibits a pseudocapacitive signature, characterized by a broad peak centered at approximately 0.8 V (Fig. 3b).

This feature is attributed to the superimposition of the individual voltammograms originating from CPE-K and $Ti_3C_2T_x$. (Fig. 3d). When the scan rate is increased, the device can maintain its pseudocapacitive signature up to scan rates of up to $10,000 \, \text{mV} \, \text{s}^{-1}$ (Fig. 3d). In fact, the log-log plot of the current versus scan rate showed a b-value of $0.92 \, \text{and} \, 0.80$ for $3.8 \, \text{and} \, 15.1 \, \text{mg} \, \text{cm}^{-2}$, respectively (Fig. 3e). Such rate performance reflects the capacitive and kinetic matching of $Ti_3C_2T_x$ and CPE-K. Figure 3f shows the GCD curves of the $Ti_3C_2T_x \parallel \text{CPE-K}$ device, which exhibits non-linear behavior at various specific currents, highlighting the pseudocapacitive characteristics resulting from the combination of both $Ti_3C_2T_x$ and CPE-K. The theoretical specific capacitance of the device can be calculated using Eq. (4)⁴²:

$$C_{s,device} = \frac{(C_{s+}m_+)(C_{s-}m_-)}{(C_{s+}m_+ + C_{s-}m_-)(m_+ + m_-)}$$
(4)

where C_s is the specific capacitance of the electrode (82 F g⁻¹ for CPE-K, 235 F g⁻¹ for Ti₃C₂T_x), m is the mass of an electrode, and m_+/m_- is the CPE-K:Ti₃C₂T_x ratio of 3.0. According to the GCD data, the maximum C_s of the cell is 32 F g⁻¹, which is close to the theoretical value of 31 F g⁻¹ calculated from Eq. (4).

EIS was carried out at a cell voltage of 0.0 V to probe the behavior of the cells in their uncharged states. The results are presented as a Nyquist plot in Fig. 3h, which reveals the absence of any visible

semicircles in the high-frequency region. Instead, the plot transitions from a Warburg region at high frequencies to a supercapacitive response at lower frequencies. As expected, the Warburg region is more pronounced at a high mass loading, attributed to the greater diffusion length for thicker electrodes. However, despite the fourfold increase in mass loading, the minor expansion of the Warburg region suggests enhanced ion accessibility to the electrode, even with the thicker electrode. We conducted cycling stability measurements by using repeated GCD cycles at 25 A g⁻¹ for the low mass loading device which has a capacitance retention of 81% after 30,000 cycles. This cycling performance is slightly lower than that observed in respective three-electrode measurements, most reasonably because of overpolarization of the CPE-K or Ti₃C₂T_x electrode as the OCV may shift over time⁴³. Nonetheless, this cycling stability surpasses that of conventional batteries by an order of magnitude⁴⁴. Overall, Ti₃C₂T_x asymmetric device exhibits promising results, attributed to its high rate capability and extensive operating voltage window in aqueous electrolytes.

Electrochemical characterization of practical $\text{Ti}_3\text{C}_2\text{T}_x$ | | CPE-K devices

Two types of cells were fabricated to demonstrate the practicality of $Ti_3C_2T_x|\mid$ CPE-K pseudocapacitors: a pouch cell with a liquid electrolyte (1.0 M H_2SO_4) and a solid-state device using a polyvinyl alcohol

(PVA)/H₂SO₄ gel electrolyte. The pouch cell serves as a functional device, although it is not the sole viable device architecture. Alternative devices, such as microsupercapacitors and/or interdigitated supercapacitors, are also feasible; though the pouch cell offers greater practicality. For the pouch cell and solid-state device, graphite foils were used as current collectors and cut to the appropriate size (Fig. S13). To deposit the active materials onto the graphite foils, aqueous solutions of Ti₃C₂T_x or CPE-K were drop-cast onto the graphite foils and dried under ambient conditions. The Ti₃C₂T_x and CPE-Kcoated graphite foils were used as electrodes without further modifications. For the pouch cell, a glass fiber separator was sandwiched between the electrodes and the overall device was placed in a polypropylene bag. An excess of degassed 1.0 M H₂SO₄ electrolyte was injected to ensure thorough infiltration. Thereafter, the cell was sealed using a vacuum pouch sealing machine. For the solid-state device, PVA/H₂SO₄ gel electrolyte (~140 μL cm⁻²) was deposited on the electrodes and allowed to dry in a 50 °C oven. When the gel electrolyte was dry, a small amount of additional liquid gel electrolyte was applied to serve as "glue" and the electrodes were sandwiched together and clamped between two glass slides before drying in oven. Both the pouch cell and solid-state device have a thickness of 0.6 mm (Fig. S13).

The pouch cell and solid-state device displayed cyclic voltammogram signatures (Fig. 4b) similar to those of the Swagelok devices, though their rate performance was slightly worse. In the case of the

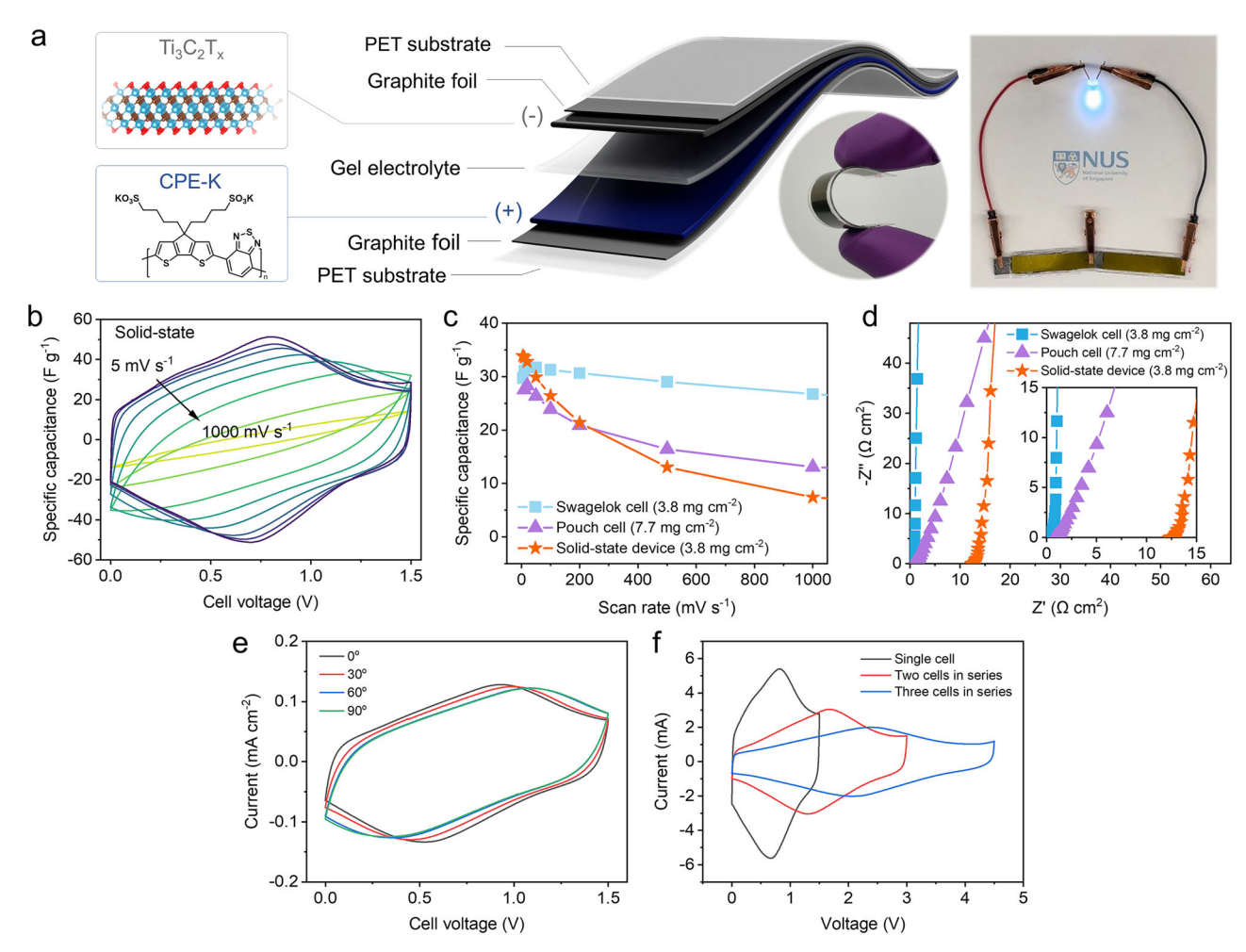


Fig. 4 | **Electrochemical performance of Ti**₃C₂T_x|| **CPE-K devices. a** Graphical scheme illustrating the fabrication Ti₃C₂T_x|| CPE-K solid-state device. **b** Cyclic voltammograms Ti₃C₂T_x|| CPE-K solid-state device at 3.8 mg cm⁻² from 5 to 1000 mV s^{-1} . **c** Rate performance of Ti₃C₂T_x|| CPE-K pouch cell (1.0 M H₂SO₄) and solid-state device compared to ideal Swagelok device. **d** Nyquist plot of

 $Ti_3C_2T_x\mid\mid$ CPE-K pouch cell and solid-state device compared to ideal Swagelok device. **e** Cyclic voltammograms of $Ti_3C_2T_x\mid\mid$ CPE-K solid-state device at different bending angles. **f** Cyclic voltammograms of a single, two, and three $Ti_3C_2T_x\mid\mid$ CPE-K solid-state device in series at a scan rate of 10 mV s⁻¹.

pouch cell, this could be attributed to the higher mass loading, while for the solid-state device, the diminished performance is likely due to its higher internal cell resistance. This was confirmed by EIS measurements, where the solid-state device showed a higher ESR (0.8 Ω cm²) than the pouch cell (12.5 Ω cm²) as indicated by the x-coordinate at the intercept on the real axis of the Nyquist plot (Fig. 4d). This increase in internal resistance can be attributed to a poorer electrodeelectrolyte interface, a common issue in devices utilizing gel electrolytes due to limited ionic conductivity and insufficient contact between the active materials and the electrolyte⁴⁵. It is worth noting that the pouch cell displayed a slope line angle of approximately 60-70 degrees in the Nyquist plot, indicative of non-ideal capacitive behavior and the presence of interfacial resistances or heterogeneities in the pouch cell. The cycling stability of the Ti₃C₂T_x|| CPE-K pseudocapacitor in a pouch cell configuration was tested, showing 80% capacitance retention after 6000 cycles (Fig. S12). We note that the pouch cell exhibited lower cycling performance compared to the Swagelok cell, likely due to the non-optimized laboratory-scale fabrication. However, the higher cycling stability observed in the Swagelok cell highlights the potential for further optimization of the pouch cell to enhance its long-term performance.

Both pouch cell and solid-state devices could achieve a high areal capacitance at 225 mF cm⁻² and 122 mF cm⁻² at mass loadings of 7.7 mg cm⁻² and 3.8 mg cm⁻², respectively (Fig. S12). A bending test was conducted on the solid-state device, demonstrating its flexibility. The device could bend up to 90 degrees without losing significant capacitance, making it suitable for flexible electronics (Fig. 4e). The maximum areal energy (power) densities were 70.0 μWh cm⁻² (8.4 mW cm $^{\!-2}\!$) for the pouch cell and 38.0 $\mu Wh~cm^{\!-2}$ (1.8 mW cm $^{\!-2}\!$) for the solid-state device, surpassing many state-of-the-art asymmetric devices based on pseudocapacitive materials (Fig. 4g). Notably, the maximum power (160 mW cm⁻²) of our pouch cell not only exceeds that of reported pseudocapacitors but also that of micro-EDLCs using ionic liquid as the electrolytes. EDLCs with ionic liquids normally show much higher energy and power compared to those with aqueous electrolytes due to the larger voltage window^{41,46}. Our pseudocapacitor in an aqueous electrolyte demonstrates both higher areal energy and power than EDLCs, benefiting from the great kinetics of the full cell with large electrode mass loading. For context, the gravimetric energy densities of the cells were approximately 10 Wh kg⁻¹, which is comparable to commercial carbon-based supercapacitors. However, the devices have higher maximum power densities, up to 300 kW kg⁻¹, when compared to commercial supercapacitors, see Fig. S14. The 1.5 V electrochemical window, achieved through the asymmetric $Ti_3C_2T_x||$ CPE-K configuration, exceeds the water decomposition voltage of 1.23 V, and is consistent with voltage windows typically observed in asymmetric devices. Despite the relatively narrower voltage window, our devices demonstrate high areal energy density, owing to the high areal capacitance and enhanced rate capability of CPE-K, which ensures high power density. It is worth noting that many high-voltage electrolytes, such as organic systems or water-in-salt electrolytes, often suffer from lower conductivity, which can reduce rate performance, and extending the working voltage window may compromise cycling stability. While increasing the voltage window can enhance energy density, it also introduces trade-offs that can impact overall performance. Nevertheless, the high areal performance with aqueous electrolyte, as well as the additive-free and water-based fabrication processes, makes the $Ti_3C_2T_x||$ CPE-K pseudocapacitor promising for practical electrochemical energy storage applications.

The pouch cell design is inherently practical and widely adopted in commercial energy storage applications due to its scalability, cost-effectiveness, and ease of fabrication⁴⁷. It allows for a straightforward assembly process and efficient integration into various devices, making it a practical choice for demonstrating the capabilities of newly

developed materials. A larger pouch cell (25 × 25 mm) was also fabricated to demonstrate the potential scalability of our system, which was able to light up several LED-lights (Fig. S13h). The large pouch cell has an areal capacitance of 105 mF cm⁻², which is comparable to the low mass loading Swagelok cell, demonstrating the great potential for scale up. The large pouch cell was able to light up four LED-lights as shown in Fig. S13h. Furthermore, our pseudocapacitor is also ideal for microsupercapacitors applications, which is widely used in on-chip and wearable devices. Currently, interdigitated configurations are the most prevalent design for microsupercapacitors⁴⁸, as areal energy and power are the key performance indicators for microsupercapacitor. The interdigitated configuration enables high areal energy and power by maximizing the accessible surface area of the electrodes and reducing the ion transport distance from the bulk electrolyte, which is crucial for efficient charge transfer in thick electrodes⁴⁸. However, this configuration often requires complex fabrication processes and has limited scalability compared to pouch cells. In comparison, the CPEbased pseudocapacitor in this work, with large mass loading on both electrodes, demonstrates enhanced areal energy and power despite using pouch cell configurations. This approach offers a more practical and versatile solution for real-world applications, particularly in scenarios that require both high areal energy and high power, while also enabling simplified manufacturing.

The work herein demonstrates that CPEs are a practical and emerging class of pseudocapacitive material for energy storage applications. In particular, CPE-K can achieve an areal capacitance, up to 910 mF cm⁻² at 5 mV s⁻¹ at a loading density of 11.2 mg cm⁻². In addition, CPE-K exhibits good rate performance, maintaining 762 mF cm⁻² or 86% of its original capacitance at an increased scan rate of 100 mV s⁻¹. At a materials level, CPE-K exhibits capacitive and rate performances that are competitive or exceed that of other state-of-theart pseudocapacitive materials. CPE-K also exhibits enhanced cycling stability, whereby an 11.2 mg cm⁻² electrode maintained 84% of its original capacitance after 100,000 cycles, which is much greater than many other organic pseudocapacitors and up to 2 orders of magnitude higher than secondary battery materials. To evaluate the practicality of CPE-K, asymmetric all pseudocapacitive devices were fabricated using Ti₃C₂T_y as the negative electrode. The resulting asymmetric Swagelok cell devices achieved an operating voltage of 1.5 V in aqueous electrolyte. To further demonstrate the applicability of Ti₃C₂T_x|| CPE-K asymmetric device, a pouch cell and a solid-state device were fabricated at a mass loading of 7.7 mg cm⁻² and 3.8 mg cm⁻², respectively. The devices deliver competitive areal performance, with areal power exceeding that of EDLCs and areal energy being significantly higher. Additionally, our device also highlights the scalability and environmental sustainability, as both electrodes can be used without conductive additives and binders, and the device fabrication process is straightforward, utilizing water for processing. Overall, this work provides a platform for the future development of CPE-based electrodes for practical energy storage applications. It also demonstrates that pseudocapacitors can deliver both higher areal energy and power than EDLCs, indicating their great potential for on-chip, thin-film and flexible energy storage applications.

Methods

General information

Unless otherwise stated, all reagents were purchased from Fisher Scientific or Sigma Aldrich and used as received without further purification (>98% purity). CPDT(SO₃K)₂Br₂ and BT-B₂Pin₂ monomers were purchased from Luminescence Technologies Corporation (Taiwan) and BLD Pharmatech Ltd, respectively. TiAl₃C₂ MAX phase was purchased from Jilin 11 Technology Co. Ltd. Milli-Q water is used for all steps that require water. DMF:H₂O (4:1) solvent was made in bulk and was degassed using 3 cycles of freeze-pump-thaw, stored in a Schlenk flask, and used for the Suzuki polymerization reaction.

Synthesis of CPE-K

In a microwave vial with a stir bar, CPDT(SO₃K)₂Br₂ (0.5 g, 0.73 mmol. 1.0 eq.), BT-B₂Pin₂ (283 mg, 0.73 mmol, 1.0 eq.), K₂CO₃ (303 mg, 2.19 mmol, 3.0 eq.), and Pd(PPh₃)₄ (84 mg, 0.07 mmol, 0.1 eq.) were added and capped with a rubber septum. It was then brought out of the glovebox and using the Schlenk technique, DMF:H₂O (4:1) (15 mL) solvent was added and the microwave vial was sealed. The resulting brown mixture was heated at 80 °C for 48 h. It is worth noting that the mixture turned dark blue only after 5 min of heating. After the reaction was complete, the resulting blue mixture was poured into acetone and immediately a blue solid precipitated out. The blue precipitate was collected by centrifugation and washed with an excess amount of acetone and then MeOH until the supernatant turned colorless. The resulting blue crude product was dissolved in Milli-Q water and transferred into a dialysis tube. The crude product was dialyzed (MWCO 3500-5000) in a large beaker (3 L) for 5 days and the excess water was changed every 12 h. The fully dialyzed product was transferred into centrifuge tubes and lyophilized to provide reasonably pure CPE-K as a blue solid based on ¹H NMR (52%). NMR of the product is unavailable in D₂O due to the presence of paramagnetic radicals. Therefore, cation exchange with tetrabutylammonium bromide was done to obtain a blue solid (CPE-Bu₄N) that was soluble in DMSO. For the cation exchange, CPE-K (18 mg) was dissolved in 5 mL of Milli-Q water, while tetrabutylammonium bromide (1.76 g, 200 equivalents) was dissolved in 10 mL of Milli-Q water. The two solutions were combined and stirred for 30 min, then transferred to a dialysis tube (MWCO 3500-5000) and dialyzed against 2 L of Milli-Q water for three days, with water changed every 12 h. The partially ion exchanged CPE solution was then concentrated under vacuum, re-treated with the same amount of tetrabutylammonium bromide, and dialyzed again for three days. This process was repeated once more. Finally, CPE-Bu₄N was freeze-dried under vacuum overnight, yielding 27 mg (93%) of CPE-Bu4N as a dark blue solid, soluble in water, MeOH, DMF, and DMSO. ¹H NMR (500 MHz, DMSO-d6) δ 8.27–8.17 (m, 3H), 3.15–3.13 (m, 16H), 2.28 (brs. 4H), 2.02 (brs. 3H), 1.55–1.49 (m. 20H), 1.3–1.23 (m. 16H), 0.89 (t, 24H). M_n , GPC = 67,157, M_w/M_n = 1.01.

Synthesis of Ti₃C₂T_x

Multilayer $Ti_3C_2T_x$ was synthesized following the MILD by selective etching of Ti_3AlC_2 MAX Phase (Jilin 11 Technology Co. Ltd.) in a mixture of hydrochloric acid (HCl) and lithium fluoride (LiF)²². To a solution of 9 M HCl (20 mL), LiF (1g) was added and subsequently, Ti_3AlC_2 was added slowly and allowed to stir at 35 °C for 24 h. The resulting multilayer $Ti_3C_2T_x$ was then washed with deionized water by centrifugation until the supernatant reached a pH of -7. The $Ti_3C_2T_x$ was subsequently re-dispersed in deionized water and bath-sonicated for 1 h with argon bubbling while kept cool with ice. The resulting mixture was centrifuged at 3500 rpm (2200 × g) for 1 h to obtain the black supernatant which constituted the colloidal solution of $Ti_3C_2T_x$ which was further concentrated under reduced pressure to obtain $Ti_3C_2T_x$ ink of a concentration of approximately 12 mg mL⁻¹.

Material characterization

X-ray diffraction (XRD) patterns of samples were obtained using a Bruker D8 Advance diffractometer using Cu $K_{\alpha l}$ radiation (λ = 1.5406 Å). The morphology of the samples characterized by SEM was carried out using a JEOL JSM6700F. XPS was obtained using a Kratos AXIS Ultra DLD. Samples for SEM, XPS, and XRD were prepared by drop casting a known amount of CPE-K on to 1×1 cm gold plated silicon substrates. The "Pristine" sample was analyzed without further modifications. For the "CPE+" sample, it was immersed in 1.0 M H₂SO₄ and a constant voltage of +0.8 V was applied for 5 min. It was then removed from the electrolyte and excess electrolyte was removed using a Kimwipe. For the CPE-H sample, it was immersed in 1.0 M H₂SO₄ and a constant voltage of +0.8 V was applied for 5 min. After

5 min, a constant voltage of -0.2 V was then applied for another 5 min, removed and removed of excess electrolyte. For cross-sectional SEM, the films on the gold-plated silicon substrates were flashed-frozen in liquid nitrogen and cleaved using a diamond scribe. A lower mass loading of 1.0–4.0 mg cm⁻² and 0.6–2.4 mg cm⁻² for CPE-K and ${\rm Ti}_3{\rm C}_2{\rm T}_x$ respectively, was prepared for thickness measurements using cross-sectional SEM. Thereafter, the thickness of the mass loading characterized electrochemically was extrapolated by a linear fit of the lower mass loading.

Spectroelectrochemistry

CPE-K solution (100 μ L, 20 mg mL $^{-1}$) was spin-cast onto an ITO-coated glass slide (10 $\times50$ mm). The measurement was conducted in a glass cuvette filled with 1.0 M H₂SO₄ electrolyte and the CPE-K coated ITO glass slide as the working electrode, a Pt wire as counter electrode and a silver wire as the reference electrode. The UV-Vis spectrum was recorded while the respective potential was being held using a constant voltage using a potentiostat.

Electrochemical Quartz crystal microbalance experiment

Measurements were conducted using the QSense Analyzer, a QSense Electrochemistry Module (QEM 401), and gold sensors with a titanium adhesion layer (QSensors QSX 338) from Biolin Scientific. The experiments were performed in deoxygenated 1.0 M $\rm H_2SO_4$, continuously bubbled with argon gas. A detailed procedure for obtaining baseline QCM-D can be obtained in the literature 49 . Briefly, CPE-K was spin cast on gold coated QCM sensors. It was then placed in an electrochemical QCM flow cell and the swelling data was obtained before electrochemical doping. After obtaining baseline data, an aqeuous solution of CPE-K (100 μL , 20 mg mL $^{-1}$) was spin cast on the same sensor and used for EQCM-D analysis without further modification. Cyclic voltammetry at a scan rate of 10 mV s $^{-1}$ was applied to the sensor from the open circuit voltage to 0.6 V and back to 0.1 V vs Ag/AgCl. The resulting data was modeled using the Sauerbrey equation.

Preparation of electrodes

Glassy carbon electrodes were polished using a polishing pad, and washed with deionized water and ethanol prior to drop cast. As obtained graphite foils were cut into the desired shapes (1 × 1 cm with a small tab) and plasma treated prior to drop cast. CPE-K ink was prepared by dissolving CPE-K powder in Milli-Q water to a concentration of 20 mg mL $^{-1}$ and vortexed and bath sonicated for 5 min to ensure full dispersion. The resulting CPE-K ink was used for drop casting directly on the current collectors. The maximum volume deposited was 10 μ L and 100 μ L, respectively for glassy carbon electrodes and graphite foils, respectively. For higher mass loadings, the droplet was allowed to dry before additional deposition. For example, an 11.2 mg cm $^{-2}$ CPE-K film was made using a total of four 10 μ L deposits on glassy carbon electrodes. A similar process was used for Ti $_3$ C $_2$ T $_x$ ink to obtain Ti $_3$ C $_2$ T $_x$ films of the desired mass loading.

Preparation of Pouch cell

A glass fiber separator (thickness = $260~\mu m$) was cut and sandwiched between prepared CPE-K or $Ti_3C_2T_x$ on graphite foil electrodes (thickness = $100~\mu m$). It was inserted into a polypropylene bag and filled with 1.0 M H₂SO₄ electrolyte (150 μL for 10 ×10 mm pouch cell; 500 μL for 25 × 25 mm pouch cell). The cell was placed under a mild vacuum for 15 min to encourage wetting of the electrodes. The bag was sealed using a pouch sealing machine.

Preparation of solid-state device

A 1 × 4 cm graphite foil was anchored on a PET film with double Kapton tape. Using a pencil, a 1 × 3 cm area was marked and the respective CPE-K or $\text{Ti}_3\text{C}_2\text{T}_x$ aqueous solution was drop-cast on the graphite foil and allowed to dry at ambient conditions. When dried, liquid PVA/H₂SO₄

electrolyte³⁷ was deposited on the surface of the electrode on graphite foil at a loading of 140 μ L cm⁻² and allowed to dry in a 50 °C oven for 3 h. After drying, approximately 50 μ L of liquid PVA/H₂SO₄ electrolyte was applied to serve as "glue" and the two electrodes were sandwiched together between two glass slides and allowed to further dry in a 50 °C oven for another 3 h. The device was coniditoned using chronoamperometry at 1.5 V for 1 h before electrochemical characterization.

Electrochemical measurements

All electrochemical measurements are done with a VMP300 potentiostat. (BioLogic, France) at ambient conditions (~25 °C). For cyclic voltammetry (CV), a potentiostatic hold of the vertex potential was applied to the cell for 5 min to precondition the electrode. For galvonostatic charge/discharge (GCD) cycling, the voltage cut-off used was the vertex potential as determined by cyclic voltammetry. Electrochemical impedance spectroscopy (EIS) measurements were performed potentiostatically at open-circuit potential. A small sinusoidal potential signal with an amplitude of 10 mV was applied over a frequency range from 100 kHz to 10 mHz. The impedance data were collected with 6 data points per decade of frequency. Prior to measurement, the system was allowed to stabilize at open-circuit voltage for 5 min to ensure quasi-stationary conditions. For three-electrode measurements, a Swagelok cell with 150 μL of 1.0 M H₂SO₄ electrolyte, an overcapacitive activated carbon counter electrode and 3.5 M Ag/ AgCl reference electrode was used. No reference electrode calibration was performed; potentials are reported as measured versus the Ag/ AgCl electrode which was stored in 3.5 M Ag/AgCl after use.

Data availability

All data of importance for this protocol have been included either in the main manuscript or Supporting Information. Any further details related to this study can be requested from the corresponding authors. The experimental data generated in the main figures are provided in the Source Data file. Source data are provided with this paper.

References

- Raza, W. et al. Recent advancements in supercapacitor technology. Nano Energy 52, 441–473 (2018).
- Simon, P. & Gogotsi, Y. Perspectives for electrochemical capacitors and related devices. *Nat. Mater.* 19, 1151–1163 (2020).
- Shao, Y. et al. Design and mechanisms of asymmetric supercapacitors. Chem. Rev. 118, 9233–9280 (2018).
- 4. Simon, P. & Gogotsi, Y. Materials for electrochemical capacitors. *Nat. Mater.* **7**, 845–854 (2008).
- Jiang, H., Li, C., Sun, T. & Ma, J. A green and high energy density asymmetric supercapacitor based on ultrathin MnO2 nanostructures and functional mesoporous carbon nanotube electrodes. *Nanoscale* 4, 807–812 (2012).
- Wang, X. et al. Geometrically confined favourable ion packing for high gravimetric capacitance in carbon-ionic liquid supercapacitors. Energy Environ. Sci. 9, 232–239 (2016).
- Fleischmann, S. et al. Pseudocapacitance: From fundamental understanding to high power energy storage materials. *Chem. Rev.* 120, 6738–6782 (2020).
- Augustyn, V., Simon, P. & Dunn, B. Pseudocapacitive oxide materials for high-rate electrochemical energy storage. *Energy Environ. Sci.* 7, 1597–1614 (2014).
- Choi, C. et al. Achieving high energy density and high power density with pseudocapacitive materials. *Nat. Rev. Mater.* 5, 5–19 (2020).
- Li, X. et al. MXene chemistry, electrochemistry and energy storage applications. Nat. Rev. Chem. 6, 389–404 (2022).
- Wang, X. & Bannenberg, L. Design and characterization of 2D MXene-based electrode with high-rate capability. MRS Bull. 46, 755–766 (2021).

- Anasori, B., Lukatskaya, M. R. & Gogotsi, Y. 2D metal carbides and nitrides (MXenes) for energy storage. Nat. Rev. Mater. 2, 1–17 (2017).
- 13. Wang, X. et al. Influences from solvents on charge storage in titanium carbide MXenes. *Nat. Energy* **4**, 241–248 (2019).
- Lukatskaya, M. R. et al. Ultra-high-rate pseudocapacitive energy storage in two-dimensional transition metal carbides. *Nat. Energy* 2, 1–6 (2017).
- Kurra, N., Ahmed, B., Gogotsi, Y. & Alshareef, H. N. MXene-on-Paper Coplanar Microsupercapacitors. Adv. Energy Mater. 6, 1601372 (2016).
- Peng, Y.-Y. et al. All-MXene (2D titanium carbide) solid-state microsupercapacitors for on-chip energy storage. *Energy Environ*. Sci. 9, 2847–2854 (2016).
- Shao, H., Lin, Z., Xu, K., Taberna, P.-L. & Simon, P. Electrochemical study of pseudocapacitive behavior of Ti3C2Tx MXene material in aqueous electrolytes. *Energy Storage Mater.* 18, 456–461 (2019).
- Miller, J. R. & Simon, P. Electrochemical capacitors for energy management. Science 321, 651–652 (2008).
- Toupin, M., Brousse, T. & Bélanger, D. Charge storage mechanism of MnO2 electrode used in aqueous electrochemical capacitor. *Chem. Mater.* 16, 3184–3190 (2004).
- Brezesinski, T., Wang, J., Tolbert, S. H. & Dunn, B. Ordered mesoporous α-MoO3 with iso-oriented nanocrystalline walls for thin-film pseudocapacitors. *Nat. Mater.* 9, 146–151 (2010).
- 21. Boota, M. & Gogotsi, Y. MXene—Conducting polymer asymmetric pseudocapacitors. *Adv. Energy Mater.* **9**, 1802917 (2019).
- Li, K. et al. All-pseudocapacitive asymmetric MXene-carbonconducting polymer supercapacitors. *Nano Energy* 75, 104971 (2020).
- Lee, W., Seo, J. H. & Woo, H. Y. Conjugated polyelectrolytes: A new class of semiconducting material for organic electronic devices. *Polymer* 54, 5104–5121 (2013).
- Paulsen, B. D., Tybrandt, K., Stavrinidou, E. & Rivnay, J. Organic mixed ionic–electronic conductors. *Nat. Mater.* 19, 13–26 (2020).
- Vázquez, R. J. et al. Increasing the molecular weight of conjugated polyelectrolytes improves the electrochemical stability of their pseudocapacitor gels. J. Mater. Chem. A 10, 21642–21649 (2022).
- 26. Vázquez, R. J. et al. Pseudocapacitive gels based on conjugated polyelectrolytes: thickness and ion diffusion limitations. *J. Mater. Chem. A* 11, 18843–18852 (2023).
- Ponder, J. F. Jr., Österholm, A. M. & Reynolds, J. R. Conjugated polyelectrolytes as water processable precursors to aqueous compatible redox active polymers for diverse applications: Electrochromism, charge storage, and biocompatible organic electronics. Chem. Mater. 29, 4385–4392 (2017).
- Jiang, Y. et al. Recyclable conjugated polyelectrolyte hydrogels for pseudocapacitor fabrication. ACS Appl. Mater. Interfaces 16, 19968–19976 (2024).
- Yip, B. R. P. et al. Conjugated polyelectrolyte thin films for pseudocapacitive applications. Adv. Mater. 36, 2308631 (2024).
- Mai, C.-K. et al. Facile doping of anionic narrow-band-gap conjugated polyelectrolytes during dialysis. Angew. Chem. Int. Ed. 52, 12874–12878 (2013).
- 31. Forse, A. C. et al. NMR study of ion dynamics and charge storage in ionic liquid supercapacitors. *J. Am. Chem.* Soc. **137**, 7231–7242 (2015).
- Cao, D. X. et al. The importance of sulfonate to the self-doping mechanism of the water-soluble conjugated polyelectrolyte PCPDTBT-SO3K. Mater. Chem. Front. 4, 3556–3566 (2020).
- Mai, C.-K. et al. Side-chain effects on the conductivity, morphology, and thermoelectric properties of self-doped narrow-band-gap conjugated polyelectrolytes. J. Am. Chem. Soc. 136, 13478–13481 (2014).
- Chen, R., Yu, M., Sahu, R. P., Puri, I. K. & Zhitomirsky, I. The development of pseudocapacitor electrodes and devices with high active mass loading. Adv. Energy Mater. 10, 1903848 (2020).

- Wu, Q. et al. Cyclic stability of supercapacitors: Materials, energy storage mechanism, test methods, and device. J. Mater. Chem. A 9, 24094–24147 (2021).
- Qiao, L. et al. Anion π-π stacking for improved lithium transport in polymer electrolytes. J. Am. Chem. Soc. 144, 9806–9816 (2022).
- 37. Jiang, Q., Kurra, N., Alhabeb, M., Gogotsi, Y. & Alshareef, H. N. All Pseudocapacitive MXene-RuO2 asymmetric supercapacitors. *Adv. Energy Mater.* **8**, 1703043 (2018).
- Downes, M., Shuck, C. E., McBride, B., Busa, J. & Gogotsi, Y. Comprehensive synthesis of Ti3C2Tx from MAX phase to MXene. *Nat. Protoc.* 19, 1807–1834 (2024).
- Ding, L. et al. MXene molecular sieving membranes for highly efficient gas separation. Nat. Commun. 9, 155 (2018).
- Ghidiu, M., Lukatskaya, M. R., Zhao, M.-Q., Gogotsi, Y. & Barsoum, M. W. Conductive two-dimensional titanium carbide 'clay' with high volumetric capacitance. *Nature* 516, 78–81 (2014).
- Van Aken, K. L., Beidaghi, M. & Gogotsi, Y. Formulation of ionicliquid electrolyte to expand the voltage window of supercapacitors. Angew. Chem. 127, 4888–4891 (2015).
- Chen, L. Y., Hou, Y., Kang, J. L., Hirata, A. & Chen, M. W. Asymmetric metal oxide pseudocapacitors advanced by three-dimensional nanoporous metal electrodes. *J. Mater. Chem. A* 2, 8448 (2014).
- Wang, L. et al. Origin of theoretical pseudocapacitance of twodimensional supercapacitor electrodes Ti3C2T2 (T = bare, O, S). J. Mater. Chem. A 7, 16231–16238 (2019).
- Sahoo, S., Kumar, R., Joanni, E., Singh, R. K. & Shim, J.-J. Advances in pseudocapacitive and battery-like electrode materials for high performance supercapacitors. *J. Mater. Chem. A* 10, 13190–13240 (2022).
- Li, X. et al. High energy flexible supercapacitors formed via bottomup infilling of gel electrolytes into thick porous electrodes. *Nat. Commun.* 9, 2578 (2018).
- Mousavi, M. P. S. et al. Ionic liquids as electrolytes for electrochemical double-layer capacitors: Structures that optimize specific energy. ACS Appl. Mater. Interfaces 8, 3396–3406 (2016).
- 47. Bhattacharjya, D., Carriazo, D., Ajuria, J. & Villaverde, A. Study of electrode processing and cell assembly for the optimized performance of supercapacitor in pouch cell configuration. *J. Power Sources* **439**, 227106 (2019).
- Liu, N. & Gao, Y. Recent progress in micro-supercapacitors with inplane interdigital electrode architecture. Small 13, 1701989 (2017).
- 49. Surgailis, J. et al. Mixed conduction in an N-type organic semiconductor in the absence of hydrophilic side-chains. *Adv. Funct. Mater.* **31**, 2010165 (2021).

Acknowledgements

X.W. acknowledges the support from the NWO open competition (OCENW.M.22.303). This research was supported by the Ministry of Education, Singapore, under its Research Center of Excellence award to the Institute for Functional Intelligent Materials (I-FIM, project No.

EDUNC-33-18-279-V12) and by the National University of Singapore start-up grant A-0004525-00-00.

Author contributions

B.R.P.Y. conceived and designed the study, prepared the figures, and drafted the manuscript. C.C. synthesized and characterized the $\rm Ti_3C_2T_x$ materials used in this work. Y.J. and D.O. contributed through manuscript proofreading and general support. G.C.B. and X.W. provided supervision, funding, and overall guidance. G.C.B. and X.W. are the corresponding authors. All authors discussed the results and commented the manuscript.

Competing interests

The authors declare no competing interests.

Additional information

Supplementary information The online version contains supplementary material available at https://doi.org/10.1038/s41467-025-63034-9.

Correspondence and requests for materials should be addressed to Guillermo C. Bazan or Xuehang Wang.

Peer review information *Nature Communications* thanks George Chen, Tingting Jiang, and the other, anonymous, reviewer for their contribution to the peer review of this work. A peer review file is available.

Reprints and permissions information is available at http://www.nature.com/reprints

Publisher's note Springer Nature remains neutral with regard to jurisdictional claims in published maps and institutional affiliations.

Open Access This article is licensed under a Creative Commons Attribution-NonCommercial-NoDerivatives 4.0 International License, which permits any non-commercial use, sharing, distribution and reproduction in any medium or format, as long as you give appropriate credit to the original author(s) and the source, provide a link to the Creative Commons licence, and indicate if you modified the licensed material. You do not have permission under this licence to share adapted material derived from this article or parts of it. The images or other third party material in this article are included in the article's Creative Commons licence, unless indicated otherwise in a credit line to the material. If material is not included in the article's Creative Commons licence and your intended use is not permitted by statutory regulation or exceeds the permitted use, you will need to obtain permission directly from the copyright holder. To view a copy of this licence, visit http://creativecommons.org/licenses/by-nc-nd/4.0/.

© The Author(s) 2025